CrystEngComm

ROYAL SOCIETY OF CHEMISTRY

PAPER

View Article Online
View Journal | View Issue

Cite this: *CrystEngComm*, 2025, **27**, 3700

Excellent electrocatalytic performance of $CuCo_2S_4$ nanowires for high-efficiency overall water splitting in alkaline and seawater media†

Bo-yao Zhang,[a] Song-lin Xu,[a] Jia Li,[a] Hui-ya Zhou,[a] Xin Li,[a] Rong-da Zhao, *[a] Fu-fa Wu*[a] and Depeng Zhao*[b]

Received 21st January 2025,
Accepted 17th April 2025

DOI: 10.1039/d5ce00084j

rsc.li/crystengcomm

Electrode materials play a key role in enhancing the energy conversion efficiency of catalysts. Therefore, developing cost-effective, non-precious metal electrocatalysts with high catalytic activity for water splitting is crucial. The hydrogen evolution reaction (HER) and oxygen evolution reaction (OER) are critical for water splitting. Despite their theoretical advantages, ternary metal sulfides face practical limitations, necessitating continuous optimization to fully unlock their potential. In this study, $CuCo_2S_4$ nanowires are synthesized through a two-step hydrothermal process followed by air annealing. $CuCo_2S_4$ demonstrates excellent HER performance, with a low overpotential of 86.2 mV in 1 M KOH to achieve a current density of 10 mA cm^{-2}, which slightly increases to 91.2 mV in 1 M seawater KOH. For the OER, the overpotential decreases from 282.8 mV in KOH to 255.6 mV in seawater. Additionally, the sample exhibits a low cell voltage of 1.7175 V at 50 mA cm^{-2}. Chronoamperometry tests further confirm its stability.

1. Introduction

As energy and environmental crises intensify, exploring sustainable and clean energy sources to replace traditional fossil fuels became a major focus in the past decade.[1–6] Hydrogen, as a clean energy source, is viewed as a suitable energy carrier to replace fossil fuels in transportation and renewable energy storage.[7] Water electrolysis is an effective method for hydrogen production. Water electrolysis involves two half-reactions: the anodic oxygen evolution reaction (OER) and the cathodic hydrogen evolution reaction (HER), which together complete the process, driven by energy from an external power source. Both half-reactions require kinetically efficient electrocatalysts to proceed with minimal overpotential.[8,9] Currently, Ru/Ir oxides are the most effective electrocatalysts for the OER, while Pt nanomaterials are optimal for the HER. However, the scarcity and high cost of these noble metal-based materials hinder their widespread application.[10,11] Thus, developing low-cost electrocatalysts with excellent catalytic performance is urgently needed. In recent decades, numerous studies have demonstrated that transition metal-based nanomaterials, including oxides,[12] sulfides,[13] phosphides,[14,15] and nitrides,[16] offer great potential as electrocatalysts due to their low cost, abundance, and excellent electrochemical properties. Transition metal sulfides, among these nanomaterials, attract significant attention for their superior electrocatalytic performance and high stability in catalysis.[13] Meanwhile, improvements in supercapacitors made from single metal oxides such as Co_3O_4,[17] CuO,[18] and NiO (ref. 19) have stagnated in recent years, shifting researchers' attention to mixed transition metal oxides containing multiple metal elements. These mixed oxides are preferred for their high capacitance, low resistance, rich oxidation states, and synergistic effects between multiple metal species, which enhance reversible redox reactions. Sulfidation of these oxides is another effective strategy to enhance electrocatalytic performance. Furthermore, recent research suggests that ternary metal sulfides generally exhibit richer redox reactions and higher electrical conductivity than their single metal counterparts, fueling growing academic interest in ternary mixed metal sulfides.[20] Similarly, the ternary compound $CuCo_2S_4$ exhibits superior electrochemical performance compared to the binary sulfides CuS and CoS. Owing to sulfur's lower electronegativity compared to oxygen, $CuCo_2S_4$ sulfides demonstrate better conductivity, higher electrochemical activity, and greater theoretical capacitance than their oxide counterpart $CuCo_2O_4$.[21] For instance, Li *et al.*[22] synthesized ultrathin $CuCo_2S_4$ nanosheets using a simple one-pot solvothermal method. These nanosheets act as efficient catalysts for the HER and OER in 1 M KOH, with overpotentials of 182 mV and 274 mV, respectively, at 10 mA cm^{-2}. Additionally, Hao *et al.*[23]

[a] *School of Materials Science and Engineering, Liaoning University of Technology, Jinzhou, Liaoning 121000, China. E-mail: Rongdazhaoln@126.com*
[b] *School of New Energy, Shenyang Institute of Engineering, Shenyang, Liaoning, 110136, P. R. China. E-mail: hellodepeng@163.com*

† Electronic supplementary information (ESI) available. See DOI: https://doi.org/10.1039/d5ce00084j

synthesized $CuCo_2S_4$ nanosheets using a one-step solvothermal method. With the addition of CTAB, these nanosheets exhibit superior OER catalytic performance, reaching a current density of 10 mA cm^{-2} with an overpotential of just 269 mV in 1.0 M KOH, and a remarkable Tafel slope of 41 mV dec^{-1}.

This study aims to enhance the hydrogen evolution reaction (HER) electrocatalysis of $CuCo_2S_4$ in alkaline media. A simple, convenient, and low-cost two-step hydrothermal method is used to synthesize $CuCo_2S_4$ nanowire arrays. The synergistic effects of Cu and Co, combined with the increased surface area and active sites from the nanostructure, further enhance the performance of the $CuCo_2S_4$ catalyst. The catalyst demonstrates excellent HER performance in 1 M alkaline KOH, with a low overpotential of 86.2 mV at −10 mA cm^{-2} and a Tafel slope of 109.34 mV dec^{-1}. At 50 mA cm^{-2}, the catalyst exhibits a low cell voltage of 1.7175 V. Additionally, in 1 M alkaline seawater KOH, the HER overpotential at −10 mA cm^{-2} is only 91.2 mV, an increase of just 5 mV compared to the KOH solution, with a Tafel slope of 104.82 mV dec^{-1}. Notably, after 12 hours of cycling, the HER overpotential decreases from 131.7 mV to 116.3 mV. Regarding oxygen evolution reaction (OER) performance, the overpotential decreases from 282.8 mV in KOH to 250.3 mV at 10 mA cm^{-2}. The double-layer capacitance (C_{dl}) values for the OER, measured at 0.1008 mF cm^{-2} and 0.1098 mF cm^{-2}, indicate excellent active site availability and outstanding reaction kinetics.

2. Experimental section

2.1. Materials

Copper(II) nitrate trihydrate [$Cu(NO_3)_2{\cdot}3H_2O$, 99%], cobalt(II) nitrate hexahydrate [$Co(NO_3)_2{\cdot}6H_2O$, 99%], ammonium fluoride (NH_4F, 96%), urea (H_2NCONH_2, 99.5%), sodium sulfide nonahydrate ($Na_2S{\cdot}9H_2O$, 98%), potassium hydroxide (KOH), absolute ethanol (C_2H_6O, 99.5%), hydrochloric acid (HCl), and nickel foam were all of analytical grade and purchased from Sigma-Aldrich. No further purification was required for these chemicals.

2.2. Preparation of $CuCo_2S_4$ nanosheets

Nickel foam was first pre-treated by cleaning in an ultrasonic cleaner, alternating between absolute ethanol and deionized water for six cycles. Afterward, the foam was dried in an oven at 60 °C for 24 hours.

Two types of $CuCo_2S_4$ nanosheets were synthesized using a two-step hydrothermal method (Scheme 1). In the first step, 4 mM $Cu(NO_3)_2{\cdot}3H_2O$, 4 mM $Co(NO_3)_2{\cdot}6H_2O$, 5 mM NH_4F, and 5 mM urea were dissolved in water. The pre-treated nickel foam (4 × 4 cm) and the solution were placed in a 100 mL autoclave and heated at 150 °C for 7 hours. After natural cooling, the precursor was washed with ethanol and deionized water, then dried at 60 °C for over 12 hours. In the second step, 0.35 g Na_2S was dissolved in 60 mL deionized water, stirred for 45 minutes, and then placed with the nickel foam in an autoclave. The reaction was conducted at 120 °C for 4 hours, followed by natural cooling, washing, and drying. Finally, the product was calcined at 350 °C for 2 hours. The resulting product was labeled $CuCo_2S_4$ (1 : 1-S), while the unsulfurized product was labeled $CuCo_2O_4$ (1 : 1).

For the second type of $CuCo_2S_4$ nanosheet, 5 mM $Co(NO_3)_2{\cdot}6H_2O$ was used, yielding a Cu ratio Co of 1 : 1.25. The products were labeled $CuCo_2O_4$ (1 : 1.25) and $CuCo_2S_4$ (1 : 1.25-S), respectively.

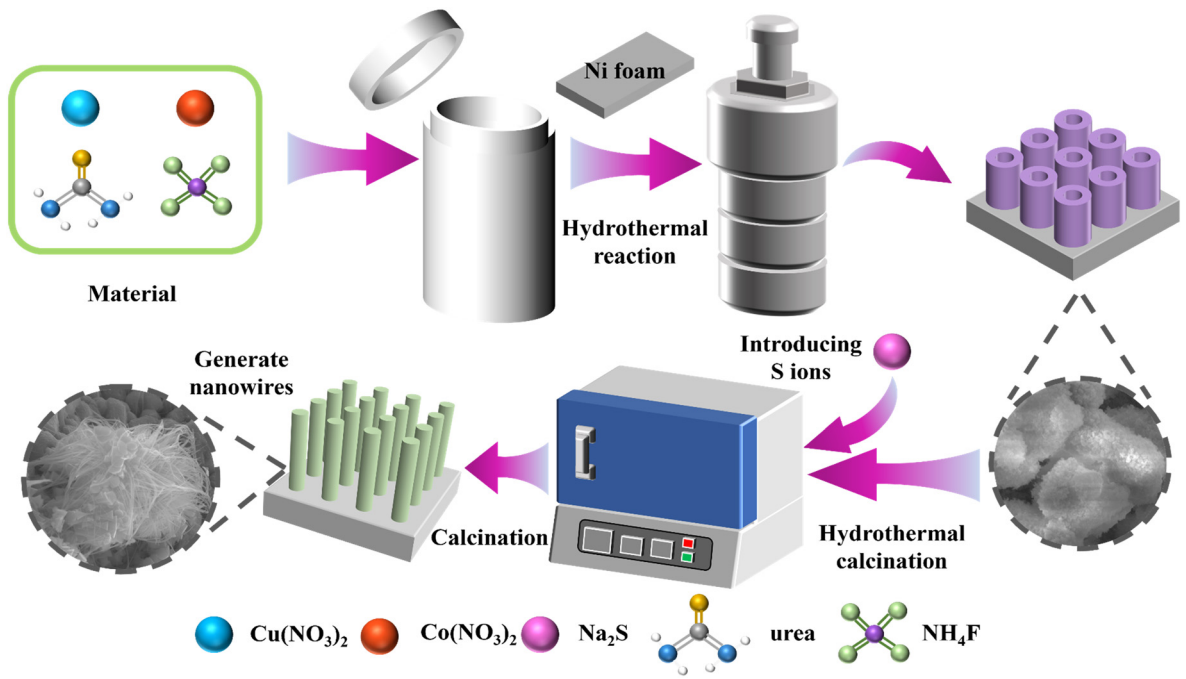

Scheme 1 Schematic diagram showing the synthesis process of $CuCo_2S_4$ on nickel foam.

2.3. Material characterization

The crystal structure of the samples was characterized by X-ray diffraction (XRD, Shimadzu-7000, Cu Kα). X-ray photoelectron spectroscopy (XPS, ESCALAB 250 with an Al Kα source) was used to analyze surface chemical states and provide qualitative and quantitative elemental information. The morphology of the samples was examined by scanning electron microscopy (SEM, Gemini 300-71-31) and transmission electron microscopy (TEM, JEM-2100 PLUS). Results showed well-defined microstructures.

2.4. Electrocatalytic performance characterization

All electrochemical tests were performed on a Chenhua electrochemical workstation (CHI660e). The tests were carried out in 1 M KOH (pH = 13.7) and 1 M seawater alkaline KOH (pH = 13.51) solutions as electrolytes. A three-electrode setup was used, consisting of a Hg/HgO reference electrode, graphite rod and Pt counter electrodes, and the samples (0.5 cm × 0.5 cm) as the working electrode. Linear sweep voltammetry (LSV) curves were adjusted with 90% IR compensation. Potentials were converted to a reversible hydrogen electrode (RHE) using the Nernst equation: $E_{RHE} = E_{Hg/HgO} + 0.059 \times pH + 0.098$. The OER overpotential (η) was calculated as $\eta = E_{RHE} - 1.23$ V.

3. Results and discussion

The phase composition of the samples is first characterized by XRD, as shown in Fig. 1. Peaks at 2θ values of 44.4°, 51.6°, and 76.1° correspond to strong diffraction peaks from the Ni foam substrate (JCPDS no. 04-0850). Strong diffraction peaks of $CuCo_2S_4$ at 2θ values of 26.6°, 31.2°, 38°, 47.5°, and 54° are indexed to the (022), (113), (004), (224), and (044) crystal planes of $CuCo_2S_4$ (JCPDS no. 00-042-1450). After the second hydrothermal sulfuration, diffraction angles at 19.02°, 32.4°, 37.36°, and 46° correspond to the (211), (141), (034), and (630) crystal planes of Cu_2S (JCPDS no. 01-073-6145), indicating partial formation of Cu_2S, with excess Cu in the +1 oxidation state. These results suggest that S atoms fully replaced O atoms in the $CuCo_2O_4$ precursor.

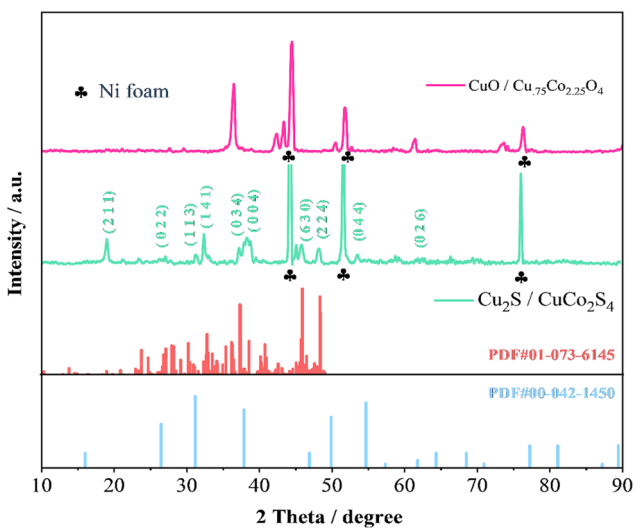

Fig. 1 XRD patterns of the $CuCo_2S_4$ (1 : 1-S) sample and its precursor.

SEM is employed to examine the changes in microscopic morphology during the conversion of copper–cobalt oxides to copper–cobalt sulfides. As shown in the SEM images (Fig. S1a† and 2a), the coral-like nanoblock-aggregated structure of $CuCo_2O_4$ transforms after sulfuration, forming numerous nanowires. The formation of nanowires significantly increases the contact area between the electrolyte and the catalyst, enhancing the electrocatalytic reaction kinetics. The remaining nanoblocks continue to contribute to charge storage, a key factor in the improved electrocatalytic performance of the copper–cobalt sulfide sample. In the higher-magnification image (Fig. S1b†), the nanoblocks exhibit a uniform layered stacking distribution, while Fig. 2b shows a cross-arranged structure of nanoblocks and nanowires. The nanowires primarily extend outward from the nanoblock centers and surround the blocks, promoting charge transfer due to the fine nanowire structures at the periphery. TEM is used to analyze the microstructure of the $CuCo_2S_4$ (1 : 1-S) sample. Fig. 2c reveals that the overall structure is dendritic. Fig. 2d, a high-magnification TEM image of the red-highlighted region from Fig. 2c, more clearly shows the tip shapes of the protruding parts. In the HRTEM image (Fig. 2e), distinct lattice fringes can be seen. The lattice spacing corresponding to the (022) plane is 0.3218 nm, while 0.2198 nm corresponds to the (224) plane of the sample. Fig. 2f shows elemental mapping of the $CuCo_2S_4$ (1 : 1-S) sample, indicating the uniform distribution of Cu, Co, and S throughout the material.

The HER performance of the electrocatalysts is evaluated in a three-electrode system with 1.0 M KOH alkaline electrolyte. As shown in Fig. 3a, $CuCo_2S_4$ (1 : 1-S) exhibits a lower overpotential (86.2 mV at −10 mA cm^{-2}) compared to $CuCo_2O_4$ (1 : 1), $CuCo_2O_4$ (1 : 1.25), and $CuCo_2S_4$ (1 : 1.25-S), while the Pt/C catalyst shows an overpotential of 44.2 mV at −10 mA cm^{-2}. The bar chart in Fig. 3b highlights the overpotential differences, showing the lower η_{10} and η_{50} values of $CuCo_2S_4$ (1 : 1-S). Kinetic factors are crucial, and Tafel plots for the samples are generated (Fig. 3c). $CuCo_2S_4$ (1 : 1-S) exhibits a Tafel slope of 109.34 mV dec^{-1}, significantly lower than that of $CuCo_2O_4$ (1 : 1) (135.02 mV dec^{-1}), $CuCo_2O_4$ (1 : 1.25) (133.19 mV dec^{-1}), and $CuCo_2S_4$ (1 : 1.25-S) (115.45 mV dec^{-1}) In alkaline electrolytes, the hydrogen evolution reaction (HER) can be divided into three steps.[24] The Tafel slope corresponding to the Volmer reaction is approximately 120 mV dec^{-1}, the Heyrovsky reaction typically exhibits a Tafel slope of 40 mV dec^{-1}, and the Tafel reaction has a slope of 30 mV dec^{-1}. The $CuCo_2S_4$ (1 : 1-S) sample shows a Tafel slope around 120 mV dec^{-1}, indicating that it primarily follows the Volmer–Heyrovsky mechanism, with the reaction rate being determined by the Volmer step ($H_2O + e^- \rightarrow H_2 + OH^-$).[25] A lower Tafel slope improves charge transfer resistance and kinetic rate control. To further investigate the catalyst's activity, double-layer capacitance (C_{dl}) is used to estimate the electrochemical active surface area (ECSA)

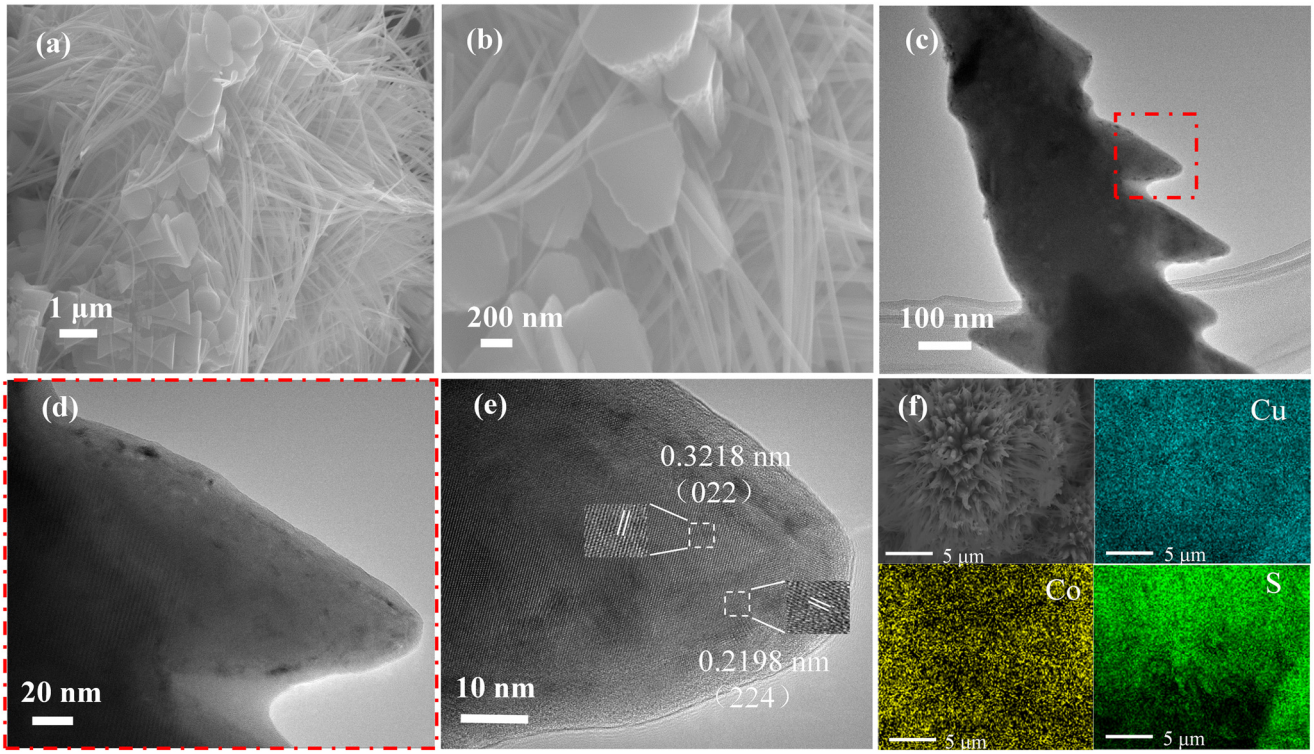

Fig. 2 Morphology and structure characterization of the as-prepared products. (a and b) SEM images of $CuCo_2S_4$ (1 : 1-S). (c–e) TEM images of the $CuCo_2S_4$ (1 : 1-S) samples. (f) elemental mapping of the $CuCo_2S_4$ (1 : 1-S) samples.

(Fig. 3d). $CuCo_2S_4$ (1 : 1-S) exhibits a higher ECSA, with a C_{dl} of 0.02 mF cm^{-2}. The Nyquist plot (Fig. 3e) is commonly used to analyze the electrochemical impedance spectroscopy (EIS) of electrocatalysts. In the high-frequency region of the Nyquist plot, $CuCo_2S_4$ (1 : 1-S) displays a small semicircle, indicating low charge transfer resistance on the electrode surface. A smaller semicircle indicates lower charge transfer resistance and faster electrochemical reaction kinetics. The low-frequency region can be referenced with the following equation.[26]

$$Z = R_s + R_{ct} + \sigma_w \omega^{-1/2} \quad (1)$$

σ_w represents the Warburg factor, ω represents the angular frequency, and Z represents the diffusion resistance of OH^- ions. The $CuCo_2S_4$ (1 : 1-S) electrode exhibits a higher slope than the $CuCo_2S_4$ (1 : 1.25-S) electrode, indicating lower ion diffusion resistance. Fig. 3f shows Bode plots for the $CuCo_2S_4$ (1 : 1-S) sample at different voltages, corresponding to current densities from −10 mA cm^{-2} to −100 mA cm^{-2}. The phase angle and frequency curves reflect the dynamic response of the catalyst.[27] As the potential becomes more negative, the phase angle in the mid-frequency region significantly decreases, indicating a reduction in charge transfer resistance (R_{ct}), which accelerates charge transfer. The cycling stability of the $CuCo_2S_4$ (1 : 1-S) catalyst for the HER is tested (Fig. 3g). After 12 hours, the current decay is slow, indicating good stability. The inset on the left compares LSV curves before and after cycling, showing a trend of decreased overpotential. The inset on the right shows impedance spectra before and after cycling, with no significant changes, further demonstrating the catalyst's stability. The excellent HER performance is attributed to the microstructural changes brought by the addition of nanowires. Fig. 3h shows the Bode plot of $CuCo_2S_4$ (1 : 1-S) after cycling, with minimal differences from the pre-cycling plot, indicating continued efficient charge transfer and stability.

OER performance is analyzed using LSV curves at a scan rate of 2 mV s^{-1}. High-valence active species like Co^{3+} play a crucial role in OER performance by promoting the oxygen evolution reaction. At 50 mA cm^{-2}, the overpotential of $CuCo_2S_4$ (1 : 1-S) is 323.3 mV, higher than 289 mV of IrO_2 but significantly lower than 382.3 mV for $CuCo_2O_4$ (1 : 1), 365.3 mV for $CuCo_2O_4$ (1 : 1.25), and 330.3 mV for $CuCo_2S_4$ (1 : 1.25-S). The Ni foam substrate exhibits an overpotential of 450 mV at 50 mA cm^{-2}, indicating its negligible contribution to the electrocatalytic performance. The adsorbate evolution mechanism (AEM) serves as a traditional pathway for the oxygen evolution reaction (OER), with the scaling relationships between different reaction intermediates being widely recognized.[28] According to previous reports,[29] the active species CoOOH formed during the OER process operates *via* the adsorbate evolution mechanism, indicating its role in oxygen release. In an alkaline environment, this involves transforming OH^- ions into O_2 and water molecules. The OER necessitates a complex four-step electron/proton transfer process to complete.[30] A lower Tafel slope value can reduce the energy threshold required for the reaction,

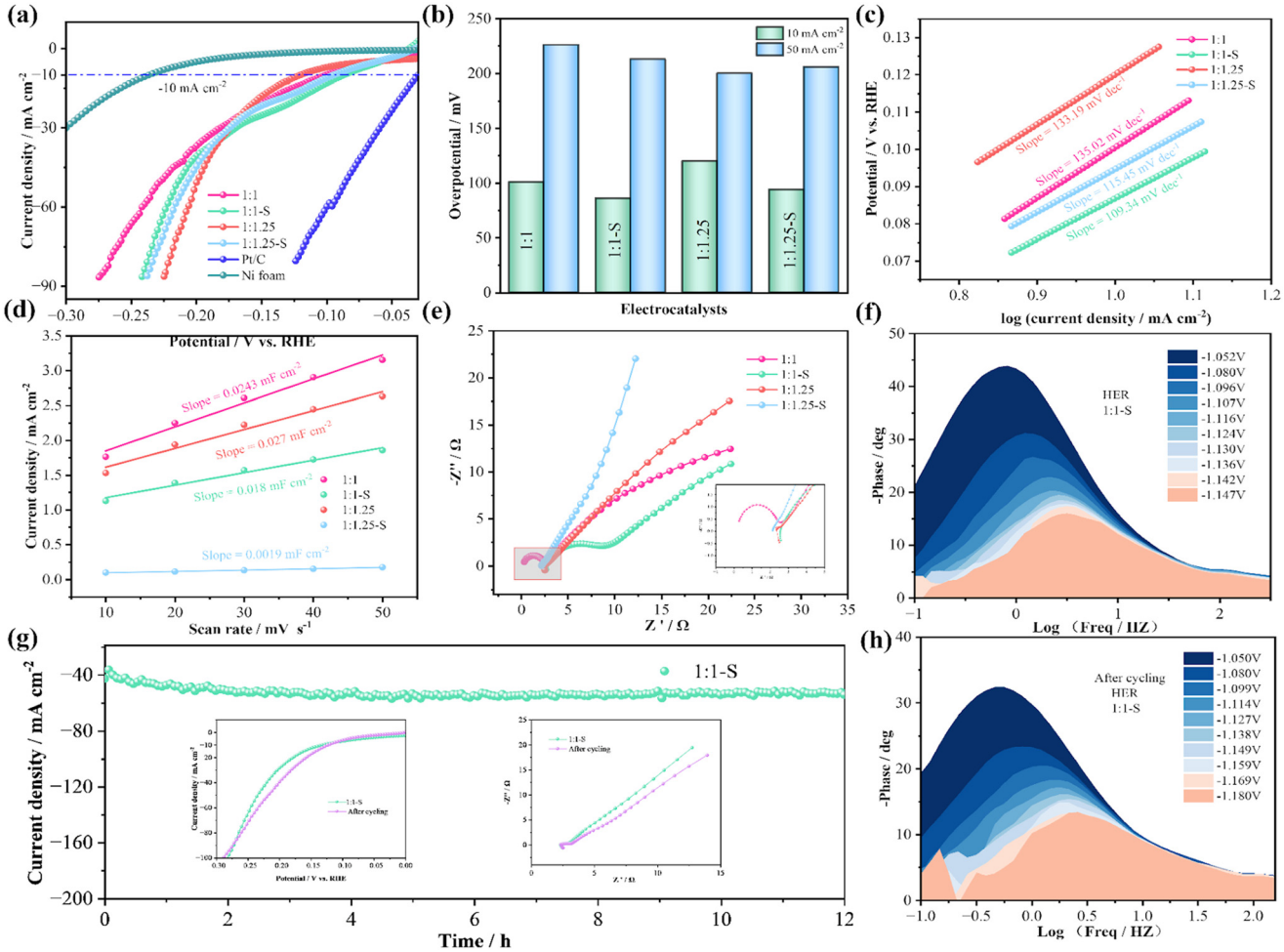

Fig. 3 HER performances in 1.0 KOH solutions: (a) polarization curves at a scan rate of 5 mV s^{-1}, (b) overpotential at different current densities, (c) Tafel plots, (d) CV curves of double-layer capacitance (C_{dl}), (e) Nyquist plots, (f) Nyquist plots at multiple voltages, and (g) chronoamperometric stability tests; the insets are LSV curves and Nyquist plots before and after electrochemical cycling. (h) Nyquist plots at multiple voltages after electrochemical cycling.

thereby exhibiting favorable reaction kinetics. The Tafel plot (Fig. 4b) is used to explore the reaction kinetics. $CuCo_2S_4$ (1 : 1-S) shows a lower Tafel slope of 89.33 mV dec^{-1} compared to $CuCo_2S_4$ (1 : 1.25-S), though it remains higher than the oxide samples. Fig. 4c compares the C_{dl} values of the electrocatalysts, revealing the catalytic activity order: $CuCo_2S_4$ (1 : 1-S) > $CuCo_2S_4$ (1 : 1.25-S) > $CuCo_2O_4$ (1 : 1.25) > $CuCo_2O_4$ (1 : 1). A larger C_{dl} value indicates a greater electrochemical active surface area (ECSA), providing more active sites for the electrocatalytic reaction. This is related to the synergistic effect between Cu^{2+} and Co^{3+}, contributing to the high catalytic activity. Fig. 4d shows the EIS spectra, where the slope in the low-frequency region indicates more efficient mass transfer in the $CuCo_2S_4$ (1 : 1-S) sample. Fig. 4e presents a radar plot showing key parameters for HER and OER performance of the four products. $CuCo_2S_4$ (1 : 1-S) clearly outperforms the other samples, particularly in terms of the OER-C_{dl} value, where it stands out significantly. The 12-hour cycling test, along with the inset showing LSV curves before and after cycling, demonstrates excellent stability, with the overpotential increasing by only 8 mV at 10 mA cm^{-2} after cycling. Subsequently, we performed X-ray diffraction (XRD) characterization on the cycled stability sample of $CuCo_2S_4$ (1 : 1-S). As shown in Fig. S3,† the peaks at 2θ values of 44.4°, 51.6°, and 76.1° are attributed to the strong diffraction peaks of the foam Ni substrate (JCPDS no. 04-0850). The prominent diffraction peaks of $CuCo_2S_4$ at 2θ values of 31.2°, 38°, 61.5°, and 68.1° can be assigned to the (113), (004), (026), and (444) crystal planes of $CuCo_2S_4$ (JCPDS no. 00-042-1450), respectively. Additionally, the diffraction angles at 28.1°, 35.2°, 46°, and 48.4° match with the (−314), (142), (630), and (−136) crystal planes of Cu_2S (JCPDS no. 01-073-6145). The appearance of new diffraction peaks proves that the material after cycling is more consistent with the standard spectrum.

Building upon previous work, X-ray photoelectron spectroscopy (XPS) was employed to further characterize the elemental composition and chemical states of the as-prepared $CuCo_2S_4$ (1 : 1-S) and its counterpart post oxygen evolution reaction (OER) cycling. Fig. 5a presents the survey spectra of both samples before and after cycling, indicating that the product consists solely of the C, O, S, Cu, and Co elements, with

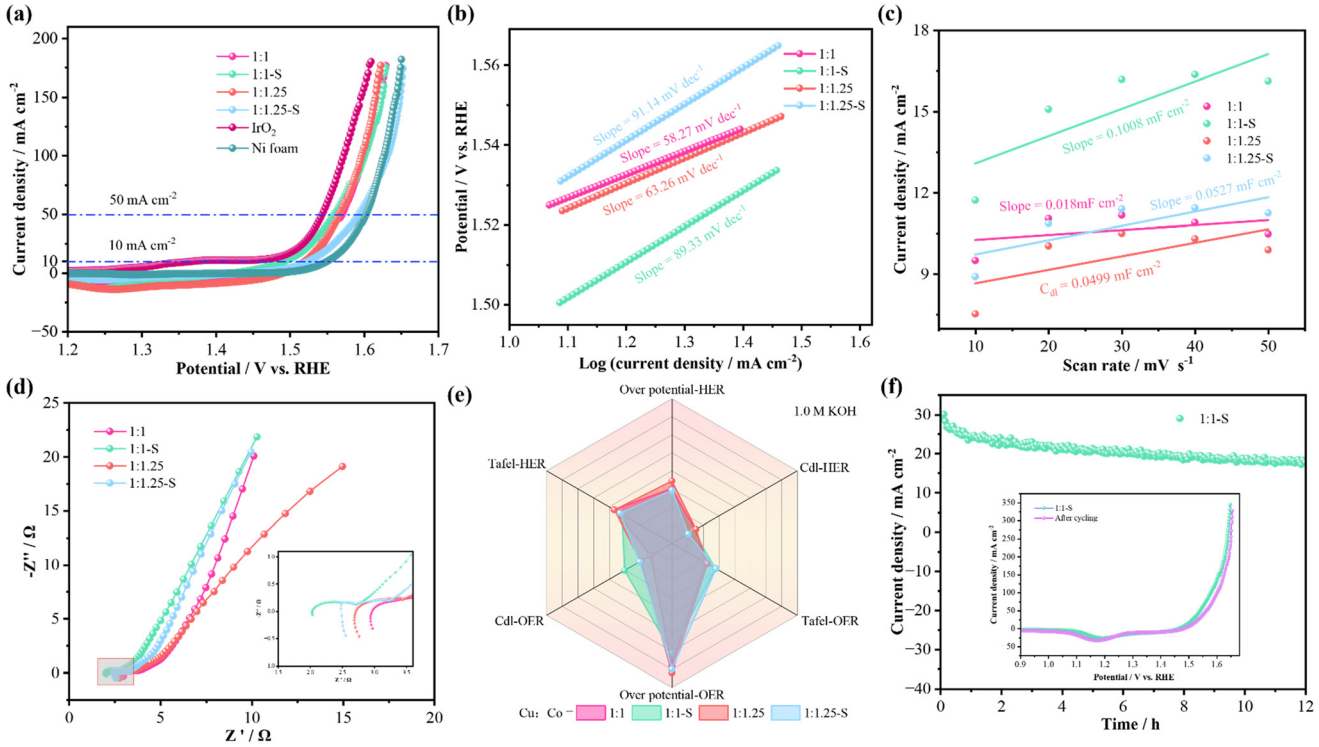

Fig. 4 OER performances in 1.0 KOH solutions: (a) polarization curves at a scan rate of 2 mV s^{-1}, (b) Tafel plots, (c) CV curves of double-layer capacitance (C_{dl}), (d) Nyquist plots, (e) radar chart, and (f) chronoamperometric stability tests; the insets are the LSV curves before and after electrochemical cycling.

no other impurities detected. The inset pie chart illustrates the atomic percentages of Cu, Co, and S, accounting for 8.2%, 0.8%, and 4.3% respectively. Post extended cycling, significant increases in the C 1s and O 1s peaks were observed alongside minor reductions in the Cu, Co, and S contents, which is primarily attributed to the leaching out of reactants during testing, thereby reducing their concentrations. Fig. 5b shows the Cu 2p spectrum of the prepared sample. Given that the peaks at 932.35 eV and 952.1 eV closely match the spin–orbit doublets of Cu $2p_{3/2}$ and Cu $2p_{1/2}$,[31] the characteristic peaks fitted at 932.35 eV and 952.1 eV in the Cu 2p spectrum can be identified as those corresponding to Cu^{2+} species. Meanwhile, the two peaks near 934.25 eV and 954.4 eV are attributed to the presence of Cu^{+}.[32,33] This observation is due to the partial formation of Cu_2S within the material. Additionally, the peaks near 942.85 eV and 962.45 eV can be attributed to shake-up satellites (denoted as Sat.). The lower spectrum, representing the Cu 2p spectrum post cycling, shows a leftward shift of approximately 2.5 eV for both Cu $2p_{3/2}$ and Cu $2p_{1/2}$ post-cycling. Furthermore, there is a notable decrease in the satellite peak associated with Cu^{2+} at the Cu $2p_{3/2}$ position, likely reflecting changes in oxidation state and chemical environment, indicating the pivotal role of Cu^{2+} in overall OER performance. This reduction suggests the consumption of Cu^{2+} during testing, yet the energy difference between the main peaks remains around 20 eV, showing no significant alteration. As shown in Fig. 5c, the Co 2p spectrum can be interpreted as comprising two spin–orbit doublets and two shake-up satellites, indicative of the coexistence of two oxidation states, Co^{3+} and Co^{2+}.[34] The Co 2p spectrum includes two peaks at lower binding energies (Co $2p_{3/2}$) and two at higher binding energies (Co $2p_{1/2}$). The two strong sharp peaks located at 780.78 eV and 796.98 eV are attributed to the presence of Co^{3+}, whereas the peaks around 782.58 eV and 801.58 eV are classified as representing divalent Co species.[35] Satellite peaks appear at binding energies of 787.28 eV and 804.38 eV. Post-cycling, the Co 2p spectrum exhibits minimal shifts; specifically, a 2.3 eV rightward shift for Co^{2+} associated with Co $2p_{1/2}$, whereas other peak binding energy changes are less than 0.75 eV. This indicates a trend towards lower energy levels compared to pre-cycling but shows no significant overall peak position change. However, there is an observable decrease in peak intensity suggesting reduced elemental content, which manifests as decreased coverage in the spectrum. Fig. 5d presents the S 2p spectrum before cycling, fitted into four major peaks: S $2p_{1/2}$ at 162.65 eV, S $2p_{3/2}$ at 159.45 eV, and satellite peaks near 168.05 eV. The peak at 164.5 eV is attributed to the typical metal–sulfur (M–S) bond in $CuCo_2S_4$ materials,[22] which facilitates electron transfer and enhances electrochemical activity.[23] In the post-cycling S 2p spectrum (Fig. 5d), it is noted that the binding energy of the strong sharp peak S $2p_{3/2}$ shifts from 159.45 eV to 169.15 eV, the S $2p_{1/2}$ fitted peak shifts from 162.65 eV to 168.15 eV, and the M–S bond shifts from 164.5 eV down to 164.05 eV, indicating a tendency towards weakening of the metal–sulfur bonds. This observation suggests potential structural or chemical changes in the material after prolonged OER cycling, possibly impacting its catalytic performance. The observed shifts and changes in peak intensities provide insights into the

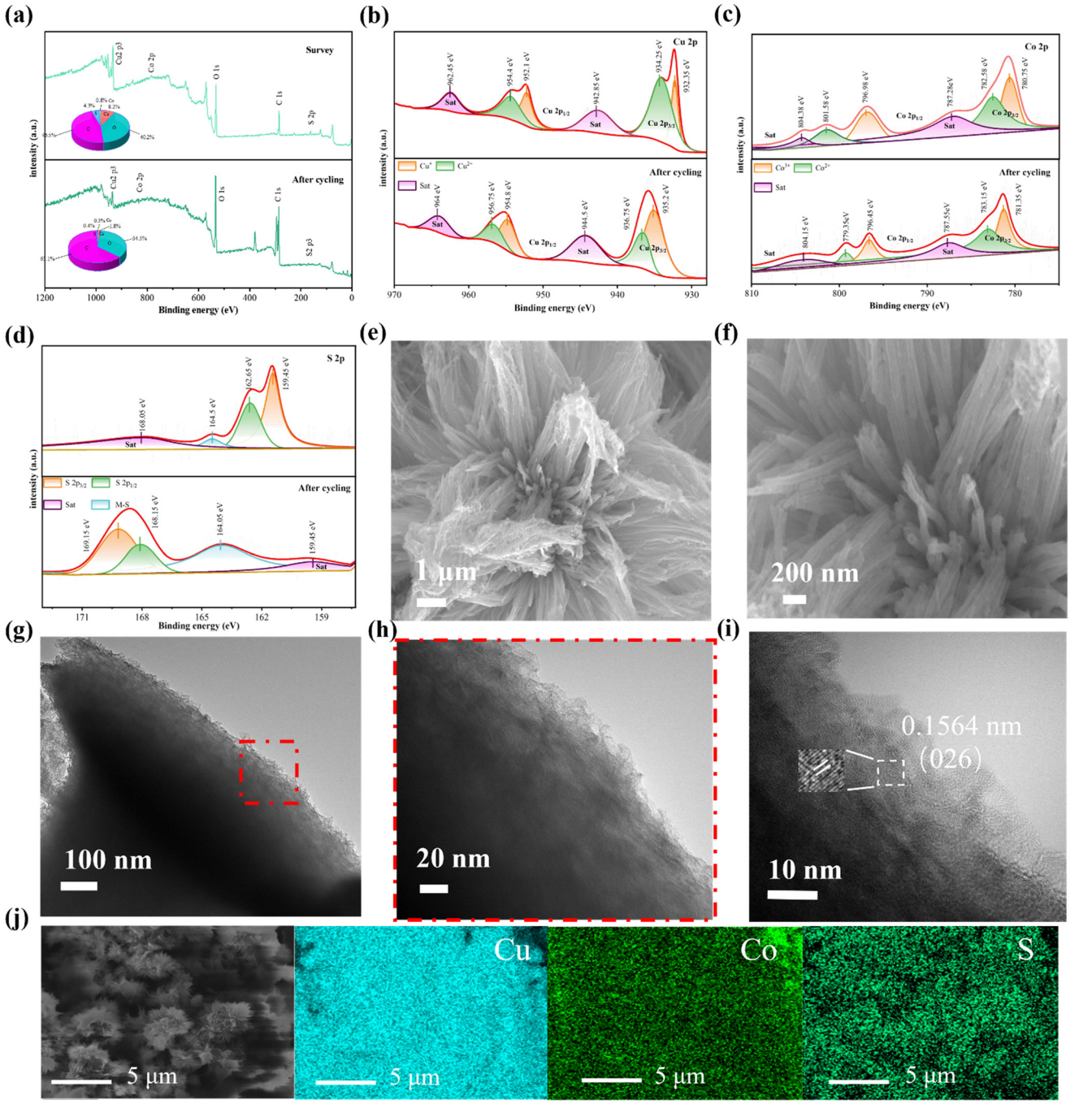

Fig. 5 XPS plot before and after cyclic stability test, morphology and structure characterization of the as-prepared products after cycle stability testing: (a) survey XPS, (b) XPS of Cu 2p, (c) Co 2p, and (d) S 2p, (e and f) SEM images of $CuCo_2S_4$ (1 : 1-S), (g–i) TEM images of $CuCo_2S_4$ (1 : 1-S) samples, and (j) elemental mapping of $CuCo_2S_4$ (1 : 1-S) samples.

transformation of oxidation states and the degradation of active sites, which are crucial for understanding the material's stability and activity over cycling. Low- and high-magnification images (Fig. 5e and f) show that after cycling, the nanowires of $CuCo_2S_4$ (1 : 1-S) became thicker and extended outward. This is related to the sample's ability to maintain efficient charge transfer rates, increasing the contact area with the electrolyte. The rougher surface observed after cycling may be attributed to corrosion in the alkaline electrolyte. TEM images (Fig. 5g and h) indicate that the $CuCo_2S_4$ (1 : 1-S) sample did not undergo significant morphological changes after cycling, except for some edge thinning due to reactant segregation, suggesting the catalyst maintains good structural stability. The HRTEM image (Fig. 5i) shows a lattice spacing of 0.1564 nm, corresponding to the (026) crystal plane. We conducted selected area electron diffraction (SAED) experiments before and after the sample stability tests. As shown in Fig. S4,† by performing supplementary analysis of the crystal structure at the atomic

level, we observed that the diffraction spots produced by the crystals after the stability test corresponded perfectly with the lattice plane parameters calibrated by transmission electron microscopy (TEM). This indicates that the sample maintained the integrity and stability of its crystal structure throughout the stability testing process. The transformation from sulfides to hydroxide oxides, a dynamic surface reconstruction process, influences the stability and activity of catalysts. During the oxygen evolution reaction (OER) process, transition metal-based materials undergo dynamic oxidation on their surfaces, forming metal oxides. This surface oxide layer can significantly lower the deprotonation energy barrier of the *OOH intermediate, thereby enhancing OER kinetics.[36–38] Through the XPS data in Fig. 5b, we clearly observe that after cycling, the area of the characteristic peak corresponding to monovalent Cu^+ is markedly higher than before cycling. Moreover, following oxidative conditions (OER) cycling, a sub-surface oxide layer is distinctly visible at the outer periphery of the sample's surface in the TEM image of Fig. 5h. These pieces of evidence indicate that the sample has undergone oxidation, generating Cu_2O, which enhances catalytic activity. As the amount of Cu_2O increases and accumulates, a passivation layer forms, which can prevent over-oxidation and corrosion, protecting the internal sulfide structure, thus enhancing material durability. This protective effect is confirmed in Fig. 5h, where no significant material precipitation or pore structures appear inside the sample. The synergistic effect of this surface oxidation and passivation explains the mechanism by which the material maintains superior performance during HER/OER cycling processes. Elemental mapping (Fig. 5j) confirmed the presence of Cu, Co, and S. The colors in the map became lighter after cycling, indicating decreased element content, corroborated by elemental composition data. Table 1 compares the electrocatalytic performance of $CuCo_2S_4$ (1 : 1-S) with previously reported results, highlighting the superior properties of the prepared sample.

In summary, we successfully synthesize $CuCo_2S_4$ samples through a simple two-step hydrothermal method followed by air annealing. The catalyst exhibits excellent performance in both the hydrogen evolution reaction (HER) and oxygen evolution reaction (OER) in 1 M alkaline solution, with a low overpotential of 86.2 mV at −10 mA cm^{-2}, and maintains high catalytic efficiency after 12 hours of cycling. Current research on water electrolysis primarily focuses on high-purity freshwater use.[46] However, freshwater makes up only 3.5% of the Earth's total water resources. As freshwater becomes increasingly scarce, the ocean presents an abundant and virtually inexhaustible supply. The hydrogen energy contained in seawater holds significant value for humanity.[47] Thus, seawater electrolysis provides a promising strategy for large-scale hydrogen production.[48] Accordingly, we conduct electrochemical tests on $CuCo_2S_4$ nanosheet samples in a 1 M alkaline seawater environment.

To evaluate the electrocatalytic performance of the samples in seawater, we first test HER performance, determining the overpotential at fixed current densities using LSV curves. As shown in Fig. 6a, $CuCo_2S_4$ (1 : 1-S) exhibits overpotentials of 91.2 mV and 112.2 mV at current densities of −10 mA cm^{-2} and −50 mA cm^{-2}, respectively, lower than $CuCo_2O_4$ (1 : 1) (126.1 mV), $CuCo_2O_4$ (1 : 1.25) (133.7 mV), and $CuCo_2S_4$ (1 : 1.25-S) (125.2 mV). Fig. 6b shows the overpotential of the catalysts at different current densities, demonstrating that $CuCo_2S_4$ (1 : 1-S) has a clear advantage at −10 mA cm^{-2}. In Fig. 6c, $CuCo_2S_4$ (1 : 1-S) shows a Tafel slope of 104.82 mV dec^{-1}, significantly lower than $CuCo_2O_4$ (1 : 1) at 168.23 mV dec^{-1}, $CuCo_2O_4$ (1 : 1.25) at 170.54 mV dec^{-1}, and $CuCo_2S_4$ (1 : 1.25-S) at 126.11 mV dec^{-1}. This indicates that $CuCo_2S_4$ (1 : 1-S) demonstrates excellent kinetics and catalytic activity. To further investigate the catalyst's activity, C_{dl} values are used to estimate ECSA. The C_{dl} value of $CuCo_2S_4$ (1 : 1-S) is 0.0403 mF cm^{-2}, higher than $CuCo_2O_4$ (1 : 1) at 0.0396 mF cm^{-2}, $CuCo_2O_4$ (1 : 1.25) at 0.0271 mF cm^{-2}, and $CuCo_2S_4$ (1 : 1.25-S) at 0.003 mF cm^{-2}. These results, combined with the overpotential and Tafel slope data, confirm that $CuCo_2S_4$ (1 : 1-S) has higher intrinsic activity, as each active site can release more catalytic activity. Overall, $CuCo_2S_4$ (1 : 1-S) exhibits excellent HER performance in alkaline seawater. Next, the OER performance in seawater is evaluated. As shown in Fig. 6e, an oxidation peak around 1.35 V *vs.* RHE indicates a pre-oxidation process during the catalytic reaction. The LSV curves show that at 10 mA cm^{-2} and 50 mA cm^{-2}, $CuCo_2S_4$ (1 : 1-S) requires

Table 1 Comparison of electrocatalytic performance of $CuCo_2S_4$ (1 : 1-S) hybrid nanostructures with previous literature reports

Materials	Performances	Electrolyte	η (mV)	Ref.
$CuCo_2S_4$	HER	1 M KOH	86.2 mV (10 mA cm^{-2})	This work
	OER		282.8 mV (10 mA cm^{-2})	
$CuCo_2S_4$	HER	1 M KOH	182 mV (10 mA cm^{-2})	39
	OER		274 mV (10 mA cm^{-2})	
$CuCo_2S_4$	HER	1 M KOH	204 mV (10 mA cm^{-2})	40
	OER		280 mV (10 mA cm^{-2})	
$CuCo_2S_4$@CoS_2	HER	1 M KOH	153 mV (10 mA cm^{-2})	41
	OER		261 mV (10 mA cm^{-2})	
NU-1000/$CuCo_2S_4$	HER	1 M KOH	93 mV (10 mA cm^{-2})	42
	OER		335 mV (10 mA cm^{-2})	
CoS/MoS_2	HER	1.0 M NaOH	121 mV (10 mA cm^{-2})	43
	OER		270 mV (10 mA cm^{-2})	
Fe,Mo–NiS/Ni_9S_8	HER	1.0 M KOH	56 mV (10 mA cm^{-2})	44
FeCoCuSx/CFF	HER	1.0 M KOH	263 mV (1000 mA cm^{-2})	45

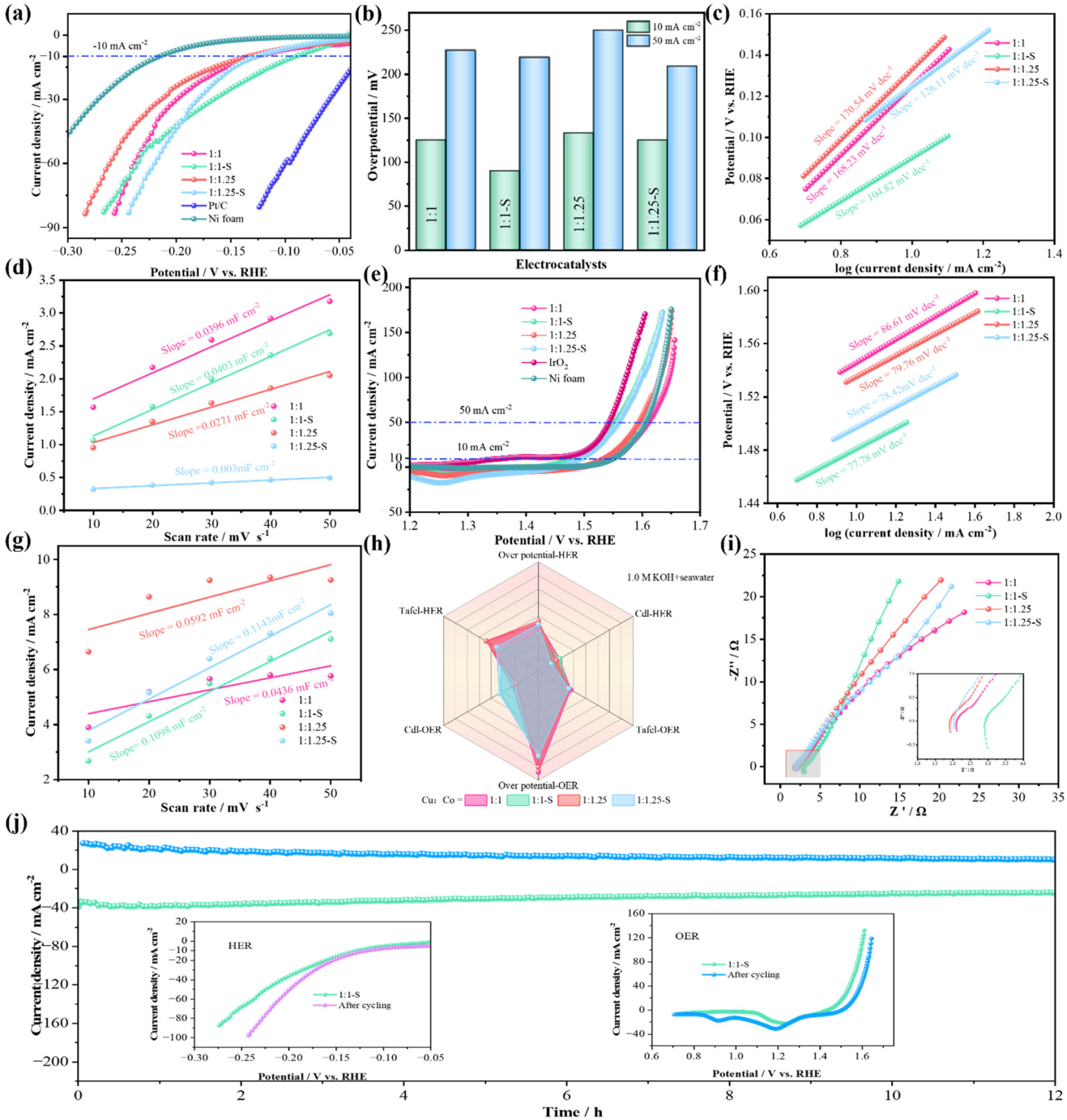

Fig. 6 Electrocatalytic performances of the electrocatalysts in alkaline seawater: (a) LSV curves for the HER, (b) overpotential at different current densities, (c) Tafel plots, (d) CV curves of double-layer capacitance (C_{dl}), (e) LSV curves for the OER, (f) Tafel plots, (g) CV curves of double-layer capacitance (C_{dl}), (h) radar chart, (i) Nyquist plots, (j) chronoamperometric stability tests; the insets are LSV curves of the HER and LSV curves of the OER before and after electrochemical cycling.

overpotentials of 250.3 mV and 323.3 mV, respectively, lower than $CuCo_2S_4$ (1 : 1.25-S) (268.3 mV and 330.3 mV), $CuCo_2O_4$ (1 : 1.25) (307.3 mV and 365.3 mV), and $CuCo_2O_4$ (1 : 1) (317.3 mV and 382.3 mV). Fig. 6f shows that $CuCo_2S_4$ (1 : 1-S) has the smallest Tafel slope at 77.78 mV dec^{-1}, lower than $CuCo_2O_4$ (1 : 1) (86.61 mV dec^{-1}), $CuCo_2O_4$ (1 : 1.25) (79.76 mV dec^{-1}), and $CuCo_2S_4$ (1 : 1.25-S) (78.42 mV dec^{-1}), indicating superior electrocatalytic reaction rates. As shown in Fig. 6g, the C_{dl} value for $CuCo_2S_4$ (1 : 1-S) is 0.1098 mF cm^{-2}, higher than $CuCo_2O_4$ (1 : 1) at 0.0436 mF cm^{-2} and $CuCo_2O_4$ (1 : 1.25) at 0.0592 mF cm^{-2} but lower than $CuCo_2S_4$ (1 : 1.25-S) at 0.1143 mF cm^{-2}. While a higher ECSA indicates more active sites, considering the overall performance, $CuCo_2S_4$ (1 : 1-S) shows a lower overpotential and Tafel slope than $CuCo_2S_4$ (1 : 1.25-S), demonstrating that each active site of $CuCo_2S_4$ (1 : 1-S) can release higher catalytic activity, suggesting better intrinsic

Table 2 ICP-MS analysis of the electrolyte solution after cycling for $CuCo_2S_4$ (1 : 1-S)

Elements	Elemental concentration ($\mu g\ L^{-1}$)
Co	193.9
Cu	7515.2
Co	183.2
Cu	7473.9
Co	195.3
Cu	7444.6

activity and catalytic efficiency. Fig. 6h presents a radar plot summarizing key parameters for the samples in alkaline seawater, showing that $CuCo_2S_4$ (1 : 1-S) outperforms the other samples in terms of both C_{dl} and overpotential. Based on impedance spectrum analysis (Fig. 6i), the higher slope of $CuCo_2S_4$ (1 : 1-S) in the high-frequency region compared to $CuCo_2S_4$ (1 : 1.25-S) indicates lower ion diffusion resistance. Finally, the stability of $CuCo_2S_4$ (1 : 1-S) in alkaline seawater is tested for both the HER and OER. As shown in Fig. 6j, $CuCo_2S_4$ (1 : 1-S) displays excellent stability after a 12-hour cycling test. The outstanding cycling lifespan is attributed to the good structural stability of $CuCo_2S_4$ (1 : 1-S). Due to the presence of chloride ions in seawater, certain side reactions can occur, such as the chlorine evolution reaction (CER) at the anode. Additionally, because the two-electron transfer process of chlorine (Cl) is very rapid, the reaction kinetics favor chlorination reactions. This makes chloride ions prone to react with OH^- to form hypochlorite, leading to chloride corrosion and the formation of insoluble precipitates, which can affect the catalyst's activity and stability. Therefore, 10 mL of electrolyte was collected for ICP-MS analysis (Table 2). The measured data showed that the average concentration of Co (cobalt) was 190.8 $\mu g\ L^{-1}$, and that of Cu (copper) was 7477.9 $\mu g\ L^{-1}$. By weighing the samples before and after cycling, it was calculated that the mass loss of the catalyst after 24 hours of electrolysis was approximately 0.8% of its initial loading. Although some dissolution of Co and Cu elements from the catalyst was detected, the fluctuation range and content of the measured data were within acceptable limits, further indicating good catalyst stability. The inset compares the overpotential before and after cycling, showing that the HER overpotential at $-10\ mA\ cm^{-2}$ decreased from 131.7 mV to 116.3 mV. However, the OER overpotential at $10\ mA\ cm^{-2}$ increased by 57 mV, likely due to the presence of chloride ions and the chlorine evolution reaction (CER) on the anode, leading to the increase in overpotential.

To further explore the electrocatalysts' potential for overall water splitting, the prepared samples (1.0 cm × 1.0 cm) are assembled as both the anode and cathode in an electrolyzer.

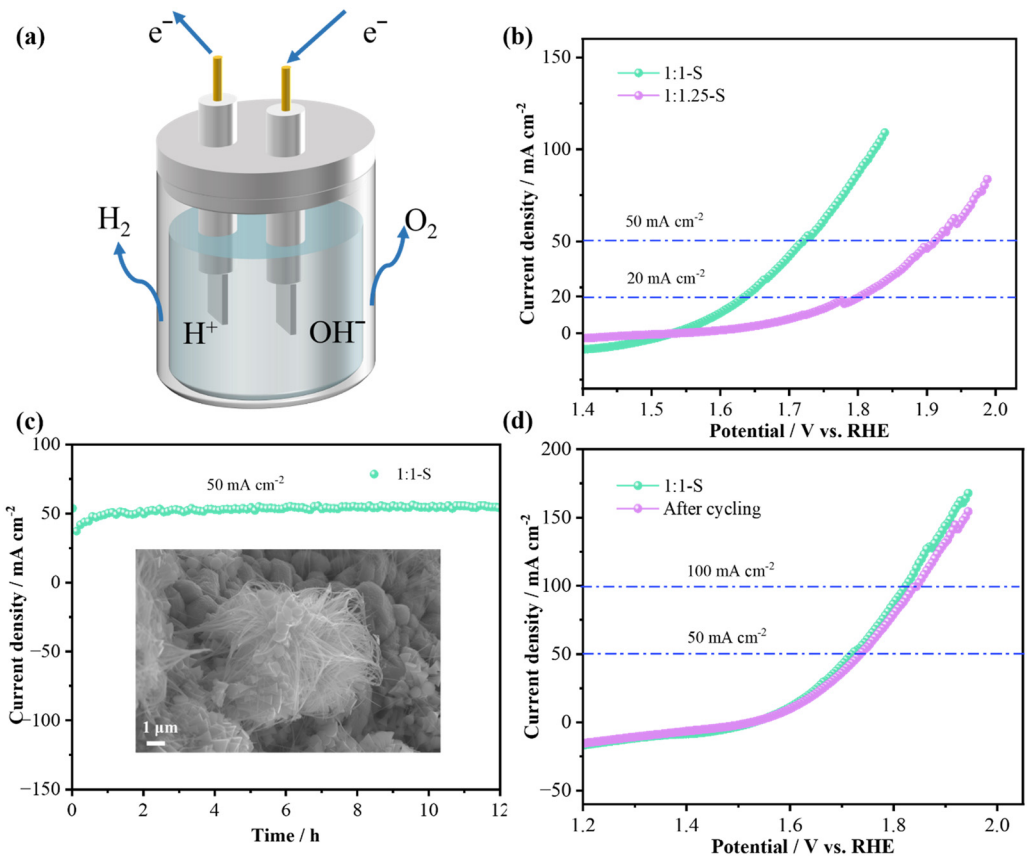

Fig. 7 Overall water splitting performance of the electrocatalysts: (a) schematic diagram of overall water splitting device, (b) LSV curves in 1.0 M KOH, (c) chronoamperometric stability tests; the insets are SEM images of $CuCo_2S_4$ (1 : 1-S), and (d) LSV curves before and after electrochemical cycling.

Fig. 7a shows the fully assembled electrolyzer. Fig. 7b compares the LSV curves for overall water splitting between activated $CuCo_2S_4$ (1 : 1-S) and $CuCo_2S_4$ (1 : 1.25-S) sulfides. The results show that $CuCo_2S_4$ (1 : 1-S) nanowire arrays exhibit higher current density and lower cell voltage. The $CuCo_2S_4$ (1 : 1-S) sample shows excellent cycling stability for overall water splitting (Fig. 7c). The inset shows that the sample's morphology after cycling remained largely unchanged, retaining the mixed structure of nanowires and nanoblocks. The LSV curves in Fig. 7d show that the cell voltage of $CuCo_2S_4$ (1 : 1-S) before and after the 12-hour cycling test is 1.7175 V and 1.736 V, respectively, indicating minimal degradation.

4. Conclusion

In summary, we successfully synthesize $CuCo_2S_4$ catalysts with a mixed nanowire array structure using a simple hydrothermal method followed by air annealing. The $CuCo_2S_4$ (1 : 1-S) sample exhibites excellent electrocatalytic performance as an electrode for the HER and OER in various electrolyte environments, showing good cycling stability, abundant active sites, and low Tafel slopes. These superior properties are attributed to the mixed structure formed by nanowire addition, ensuring rapid charge transfer and sufficient faradaic reactions. The substitution of oxygen with sulfur atoms further improves the material's conductivity. Additionally, the low cell voltage of 1.7175 V at 50 mA cm^{-2} during water splitting underscores its potential for overall water splitting applications. This study provides a reference and direction for using ternary metal sulfides as electrocatalysts in alkaline seawater.

Data availability

The data that supports the findings of this study is available from the corresponding authors upon reasonable request.

Conflicts of interest

The authors declare no conflict of interest.

Acknowledgements

This work was supported by the Project of Education Department of Liaoning Province (No. LJKMZ20220959), the Science and Technology Innovation Talent Project of Liaoning Provincial Department of Education (LJ222411632049, LJ222411632081), and the National Natural Science Foundation of China (No. 51971106).

References

1 D. P. Zhao, X. Y. Liu, W. C. Zhang, X. Wu and Y. R. Cho, *Small Methods*, 2023, **8**, 2301474.
2 W. D. Yang, R. D. Zhao, F. Y. Guo, J. Xiang, S. Loy, L. Liu, J. Y. Dai and F. F. Wu, *Chem. Eng. J.*, 2023, **454**, 140458.
3 D. P. Zhao, M. Z. Dai, H. Q. Liu, Z. X. Duan, X. J. Tan and X. Wu, *EnergyChem*, 2022, **69**, 292.
4 S. L. Xu, R. D. Zhao, R. Y. Li, J. Li, J. Xiang, F. Y. Guo, J. Qi, L. Liu and F. F. Wu, *J. Mater. Chem. A*, 2024, **12**, 15950–15965.
5 D. P. Zhao, R. Zhang, M. Z. Dai, H. Q. Liu, W. Jian, F. Q. Bai and X. Wu, *Small*, 2022, **18**, 2107268.
6 J. X. Diao, Y. Qiu, S. Q. Liu, W. T. Wang, K. Chen, H. L. Li, W. Y. Yuan, Y. T. Qu and X. H. Guo, *Adv. Mater.*, 2020, **32**, 1905679.
7 A. Z. Arsad, M. A. Hannan, A. Al-Shetwi, M. Mansue, K. M. Muttaqi, Z. Y. Dong and F. Blaabjerg, *Int. J. Hydrogen Energy*, 2022, **47**, 17285.
8 Y. J. Li, B. L. Huang, Y. J. Sun, M. C. Luo, Y. Yang, Y. N. Qin, L. Wang, C. J. Li, F. Lv, W. Y. Zhang and S. J. Guo, *Small*, 2019, **15**, 1804212.
9 R. Y. Li, S. L. Xu, Z. Q. Ai, J. G. Qi, F. F. Wu, R. D. Zhao and D. P. Zhao, *Int. J. Hydrogen Energy*, 2024, **91**, 867–876.
10 T. Tang, W. J. Jiang, S. Niu, N. Liu, H. Luo, Y. Y. Chen, S. F. Jin, F. Gao, L. J. Wan and J. S. Hu, *J. Am. Chem. Soc.*, 2017, **139**, 8320.
11 R. Abazari, A. Amani-Ghadim, A. Z. Slawin, C. Carpenter-Warren and A. Kirillov, *Inorg. Chem.*, 2022, **61**, 9514.
12 S. S. Zhang, R. Y. Li, X. Li, Y. Q. Tian, R. D. Zhao, J. Xiang, F. F. Wu and D. P. Zhao, *Mater. Res. Bull.*, 2025, **8**, 113463.
13 Y. Guo, T. Park, J. W. Yi, J. Henzie, J. Kim, Z. L. Wang, B. Jiang, Y. Bando, Y. Sugahara, J. Tang and Y. Yamauchi, *Adv. Mater.*, 2019, **31**, 1807134.
14 K. Liu, C. L. Zhang, Y. D. Sun, G. H. Zhang, X. C. Shen, F. Zou, H. C. Zhang, Z. W. Wu, E. Wegener, C. Taubert, J. Miller, Z. M. Peng and Y. Zhu, *ACS Nano*, 2018, **12**, 158.
15 H. Y. Zhou, R. Y. Li, S. Xu, B. Zhang, R. D. Zhao, X. Zhao, F. F. Wu and D. P. Zhao, *Adv. Sustainable Syst.*, 2025, **9**, 2400849.
16 N. Han, P. Y. Liu, J. Jiang, L. H. Ai, Z. P. Shao and S. M. Liu, *J. Mater. Chem. A*, 2018, **6**, 19912.
17 Y. W. Pan, F. C. Zhao, G. N. Ji, S. L. Xu, R. Y. Li, H. Y. Zhou, R. D. Zhao, D. P. Zhao and F. F. Wu, *Int. J. Hydrogen Energy*, 2025, **127**, 147–159.
18 S. Pawar, J. Kim, A. Inamdar, H. Woo, Y. Jo, B. Pawar, S. Cho, H. Kim and H. Im, *Sci. Rep.*, 2016, **6**, 21310.
19 V. Kannan, A. Inamdar, S. Pawar, H. S. Kim, H. C. Park, H. Kim, H. Im and Y. Chae, *ACS Appl. Mater. Interfaces*, 2016, **8**, 17220.
20 X. Y. Yu and X. Wen, *Adv. Energy Mater.*, 2017, **8**, 1701592.
21 S. Moosavifard, S. Fani and M. Rahmanian, *Chem. Commun.*, 2016, **52**, 4517.
22 S. N. Li, P. L. Ma, J. S. Yang, S. Krishnan, K. Kesavan, R. M. Xing and S. H. Liu, *Catalysts*, 2023, **13**, 881.
23 Z. W. Hao, P. K. Wei, Y. Yang, J. Y. Sun, Y. H. Song, D. G. Guo and L. Liu, *Appl. Surf. Sci.*, 2021, **536**, 147826.
24 C. H. Chen, D. Wu and Z. Li, *Adv. Energy Mater.*, 2019, **9**, 1803913.
25 Z. J. Wang, P. Guo, S. F. Cao, H. Y. Chen, S. N. Zhou, H. H. Liu, H. W. Wang, J. B. Zhang, S. Y. Liu, S. X. Wei, D. F. Sun and X. Q. Lu, *Appl. Catal., B*, 2021, **284**, 119725.
26 C. X. Zhao, J. N. Liu, B. Q. Li, D. Ren, X. Chen, J. Yu and Q. Zhang, *Adv. Funct. Mater.*, 2020, **30**, 2003619.
27 L. L. Guo, J. Q. Chi, T. Cui, J. W. Zhu, Y. N. Xia, H. L. Guo, J. P. Lai and L. Wang, *Adv. Energy Mater.*, 2024, **14**, 2400975.

28 X. Yuan, H. Ge, X. Wang, C. Dong, W. Dong, M. S. Riaz, Z. Xu, J. Zhang and F. Huang, *ACS Energy Lett.*, 2017, **2**, 1208–1213.
29 K. Fan, H. Zou, L. Duan and L. Sun, *Adv. Energy Mater.*, 2020, **10**, 1903571.
30 Z. Kou, L. Zhang, Y. Ma, X. Liu, W. Zang, J. Zhang and J. Wang, *Appl. Catal., B*, 2019, **243**, 678–685.
31 X. W. Xu, Y. Liu, P. Dong, P. M. Ajayan, J. F. Shen and M. X. Ye, *J. Power Sources*, 2018, **400**, 96–103.
32 H. Y. Liang, J. H. Lin, H. N. Jia, S. L. Chen, J. L. Qi, J. Cao, W. D. Fei and J. C. Feng, *Chem. Eng. J.*, 2018, **336**, 562–569.
33 S. Y. Cheng, T. L. Shi, C. Chen, Y. Zhong, Y. Y. Huang, X. X. Tao, J. J. Li, G. L. Liao and Z. R. Tang, *Sci. Rep.*, 2017, **7**, 6681.
34 S. D. Liu, Y. Yin, K. S. Hui and K. N. Hui, *Adv. Sci.*, 2018, **5**, 1800733.
35 S. Moosavifard, S. Fani and M. Rahmanian, *Chem. Commun.*, 2016, **52**, 4517.
36 J. Li, C. Guo, L. Li, Y. Gu, K. BoK-Hee and J. Huang, *Inorg. Chem. Commun.*, 2022, **138**, 109248.
37 L. L. Ji, Y. J. Wei, P. R. Wu, M. Z. Xu, T. Wang, S. Wang and Q. F. Liang, *Chem. Mater.*, 2021, **33**, 9165–9173.
38 J. J. Lv, P. P. Liu, R. S. Li, L. M. Wang, K. Y. Zhang, P. Y. Zhou, X. B. Huang and G. Wang, *Appl. Catal., B*, 2021, **298**, 120587.
39 S. N. Li, P. L. Ma, J. S. Yang, S. Krishnan, K. Kesavan, R. M. Xing and S. H. Liu, *Catalysts*, 2023, **13**, 881.
40 C. Ren, Y. J. Chen, L. Z. Du, Q. Wang, L. G. Li and G. H. Tian, *ChemElectroChem*, 2021, **8**, 1134.
41 L. H. Qian, W. W. Dong, Y. B. Cao, R. Ma, Y. Ding and X. Wang, *New J. Chem.*, 2023, **47**, 20574.
42 S. Sanati, A. Morsali and H. Garcia, *Int. J. Hydrogen Energy*, 2023, **48**, 14749.
43 K. W. Gao, M. Zhou, Y. F. Liu, S. C. Wang, F. Rong, Z. Y. Wang and J. H. Guo, *J. Colloid Interface Sci.*, 2024, **657**, 290–299.
44 Z. Zeb, Y. C. Huang, L. L. Chen, R. L. Gao, X. H. Gao, M. D. Sun and H. Q. Cai, *J. Colloid Interface Sci.*, 2025, **686**, 289–303.
45 R. X. Ren, Y. X. Wang and T. T. Li, *J. Colloid Interface Sci.*, 2025, **682**, 288–297.
46 Y. H. Chen, C. F. Liu, J. C. Xu, C. F. Xia, P. Wang, B. Y. Xia, Y. Yan and X. Y. Wang, *Small Struct.*, 2023, **4**, 2200130.
47 F. Y. Gao, P. C. Yu and M. R. Gao, *Curr. Opin. Chem. Eng.*, 2022, **36**, 100827.
48 L. B. Wu, L. Yu, F. H. Zhang, B. Mcelhenny, D. Luo, A. Karim, S. Chen and Z. F. Ren, *Adv. Funct. Mater.*, 2021, **31**, 2006484.